Nonvolatile Ferroelastic Strain from Flexoelectric Internal Bias Engineering

Wenhui Hou, Shoieb A. Chowdhury, Aditya Dey, Carla Watson, Tara Peña, Ahmad Azizimanesh, Hesam Askari, and Stephen M. Wu

Nonvolatile Ferroelastic Strain from Flexoelectric Internal Bias Engineering

Wenhui Hou[1], Shoieb A. Chowdhury[2], Aditya Dey[2], Carla Watson[3], Tara Peña[1], Ahmad Azizimanesh[1], Hesam Askari[2], and Stephen M. Wu[1,3] *

[1]Department of Electrical and Computer Engineering, University of Rochester, Rochester,

NY, 14627, USA

[2]Department of Mechanical Engineering, University of Rochester, Rochester, NY, 14627, USA

[3]Department of Physics and Astronomy, University of Rochester, Rochester, NY, 14627, USA

Abstract

Internal bias in ferroelectric materials is a well-known phenomenon that offsets the ferroelectric polarization hysteresis loop along the electric-field axes. Control over this degree of freedom could lead to new classes of ferroelectric devices, like control over the analogous concept of exchange bias in ferromagnetic devices. Currently, there lacks a systematic approach to engineer internal bias by design that allows for device-by-device control over this parameter, leading to difficulty in translating these concepts to the large-scale integration of ferroelectric electronics. In this work, the flexoelectric effect is used to engineer internal bias through the controlled deposition of stressed thin films onto ferroelectrics. Large strain gradients are generated near the surface of ferroelectric $Pb(Mg_{1/3}Nb_{2/3})_{0.71}Ti_{0.29}O_3$ (PMN-PT) single crystals, through the deposition of stressed thin film strain gauges with increasing film force (film stress × film thickness). Using this technique, it is possible to continuously tune internal bias to control ferroelastic strain applied by the ferroelectric vs. applied electric field, thereby achieving control of ferroelastic non-volatility. Flexoelectric control of internal bias is verified by density functional theory and finite element analysis using a model with no free parameters, which matches both the expected magnitude and directionality of the flexoelectric field, and then

further confirmed by piezoresponse force microscopy. This stress-induced flexoelectric effect utilizes popular strain engineering techniques already widely adopted by commercial complementary metal-oxide-semiconductor (CMOS) industrial fabrication processes, which shares the advantages of scalability and reliability with the long existing strain engineering techniques and therefore may lead to device-by-device level control of the non-volatility in ferroelectric field-effect or straintronic devices.

I. INTRODUCTION

Ferroelectric materials have numerous applications in electronic devices, such as ferroelectric random access memories (FRAMs)[1], ferroelectric field-effect transistors (FeFETs)[2] , and ferroelectric tunnel junctions (FTJs)[3,4], attributed to their unique spontaneous polarizations, which are switchable under an applied electric field. Internal bias field[5] in ferroelectric materials is a well-known phenomenon that shifts the polarization-electric field hysteresis loop along the electric-field axes [Fig. 1(a) and Fig. 1(b)]. Like the pursuit of the full control of its counterpart in ferromagnetic materials, namely exchange bias[6,7], the ability of manipulating internal bias field would also add another degree of freedom in the engineering of ferroelectric materials and devices, with applications such as logic devices and non-volatile memories. There are various approaches to induce internal bias fields, for example, through defect engineering[8-10], interface engineering[11,12], flexoelectric effect[10,13,14] and so on. However, as multiple factors (composition and stoichiometry of the material, temperature, geometry of sample and electrodes, electrical loading characteristics, …) are involved, fully understanding and manipulating internal bias are still challenging. Furthermore, since most of current techniques to manipulate internal bias are changes made to global variables or conducted through applied external forces, the idea of using these various concepts to individually tune the internal bias in individual electronic devices by design on a single chip is challenging. Since this is a prerequisite for the large-scale integration

of scalable ferroelectric devices with individually continuously tunable internal biases, it is an important milestone to achieve in achieving the same level of manufacturability ($\sim 10^{12}$ transistors per chip) as current CMOS processes.

One other commonly used application of ferroelectrics is to apply ferroelastic strain to other materials through the converse piezoelectric effect (straintronics). This method of introducing strain has its unique advantages compared to other approaches such as through lattice mismatch[15] or bending a flexible substrate[16], as it provides an electric-field controllable strain. Using ferroelastic strain, previous works have successfully demonstrated modifying the strain-sensitive material properties such as magnetization, resistivity, and ferromagnetic resonance of thin films (FeRh[17,18], $Co_{40}Fe_{40}B_{20}$[19], Co[20], Fe_2O_3[21], $Fe_{60}Co_{20}B_{20}$[22] …) or even completely switching between electronic phases of exfoliated two-dimensional materials[23] on top of a ferroelectric substrate. One main feature of ferroelastic strain is that the strain-electric field ($\mathcal{E}$-E) response is a symmetric, butterfly-like curve without remanent strain, i.e., it is volatile. However, for the purpose of non-volatile memory[24], asymmetric non-volatile strain is more desired in strain-based information storage devices. This can be achieved by breaking the symmetry either externally through asymmetric electric-field sweeping[21,22,25] or internally through introducing an internal bias field[26]. Because of the correlation between ferroelectric polarization and ferroelastic strain, when the polarization hysteresis loop is offset by the internal bias along the electric-field axis, the corresponding ferroelastic strain curve will also deviate from the symmetric butterfly-like curve and show asymmetric and non-volatile behavior, as shown in Fig. 1(c) and Fig. 1(d). Other approaches such as through a controlled polarization switching path (109° ferroelastic switching) in a specific orientation of the ferroelectric crystal[19] or electric-field-induced irreversible phase transition of ferroelectrics[27] have also been demonstrated to introducing non-volatility into ferroelastic strain. However, there also lacks a scalable method to achieve continuous engineerable control over ferroelastic non-volatility that is compatible with the large-scale

integration of devices that has the same degree of sophistication as the modern CMOS manufacturing techniques.

In this work, we show that by using controlled deposition of stressed thin films onto ferroelectric materials, we can control the internal bias through the flexoelectric effect[28,29], and in turn achieve control over the non-volatile application of ferroelastic strain. Strain engineering with stressed thin films has had an almost 20 year history in commercial CMOS integrated circuit (IC) manufacturing and been intensively modeled and verified by the process simulation with finite element analysis (FEA)[30]. With the deposition of a stressed thin film layer, typically silicon nitride, onto the transistor, strain can be introduced into the channel through stress transfer and be used to enhance electron or hole mobility[31-33]. This type of process-induced strain engineering is so widely used that almost all electronics since the 90 nm technology node in 2004 have utilized this concept to some degree [30]. By adopting a similar approach, we deposited stressed thin films on top of ferroelectric substrates to engineer nonuniform strain into the ferroelectric lattice. With a compressive (tensile) film stress, the substrate will expand (contract) locally near the interface due to the presence of the stressor, resulting in strain gradients in the ferroelectric lattice. Due to the flexoelectric effect, which is the coupling between polarization and strain gradients, there will be a positive (negative) internal bias presented in the ferroelectric material, which offsets the polarization-electric field hysteresis loop to the left (right), as shown in Fig. 1(a) (Fig. 1(b)). Because of the correlation between strain and polarization, the ferroelastic strain response will also deviate from the symmetric butterfly-like curve and show an asymmetric non-volatile behavior [Fig. 1(c) and Fig. 1(d)]. Since the strain gradients are directly proportional to controllable quantities like film stress, we also demonstrate a **continuous** tuning of the flexoelectric effect, enabling fine control of non-volatility in ferroelastic strain. Past approaches such as lattice mismatch[14,34] or inducing strain gradients using atomic force microscope (AFM) probes[35-38], have made significant strides for control of nanoscale flexoelectric effect. The unique advantage with our

approach of implementing the flexoelectric effect is that it shares the advantages of scalability and reliability with the long existing strain engineering techniques, which can be directly translated into current semiconductor manufacturing processes at the device-by-device level. Meaning these techniques can be applied to ferroelectric or straintronic devices individually with direct control over internal bias magnitude and direction to each device, much like compression and tension was controlled in strained silicon technology to enhance hole or electron mobility depending on if devices were PMOS or NMOS. These concepts therefore may have immediate benefits to the converse piezoelectric effect based straintronic applications[17-23], and the recent renaissance of deeply scaled FeFET devices[39,40], where device-level tuning of internal bias may allow for more exciting logic or memory functionality.

II. DEVICE CONFIGURATION

To test our concept, we chose (110)-oriented relaxor ferroelectric $Pb(Mg_{1/3}Nb_{2/3})_{0.71}Ti_{0.29}O_3$ (PMN-PT) single crystal as the substrate, which was reported to have both large in-plane (IP) converse piezoelectric strain response[25] and giant flexoelectric effects[41,42]. Figure 1(e) shows its rhombohedral unit cell with the 8 possible domain variants with <111> oriented polarizations. The four domain variants with IP polarizations show high remanent IP strain whereas the other four domain variants with out-of-plane (OP) polarizations show low remanent IP strain[21,25]. On top of this ferroelectric substrate, we micropatterned strain gauges made from electron-beam (e-beam) evaporated metal thin films with various film stresses. The device configurations are shown in Fig. 1(f). By poling the ferroelectric substrate with a gate voltage V_G across the PMN-PT and measuring the resistance change of the strain gauges, we were able to quantify the average IP converse piezoelectric strain response of the domains underneath the gauge. Here, the resistance changes ΔR, $\Delta R = R - R_0$, where R_0 and R are the resistance of the strain gauge at $V_G = 0$ and under a poling voltage V_G, respectively,

were converted into strain responses through the equation $\varepsilon = \frac{\Delta R/R_0}{GF}$, where $\mathcal{E}$ is the IP strain, and *GF* is the gauge factor. In Appendix A, we explained how the gauge factor was measured in detail. Each strain gauge consists of four 480-micron long metal strips with other dimensions shown in Fig. 1(g). As there is always a certain amount of intrinsic film stress in an e-beam evaporated metal thin film[43], depending on whether it is tensile stressed or compressive stressed, the film tends to contract or expand to relax the stress. However, as the film is bonded on the substrate and does not uniformly cover the whole substrate, this results in a nonuniform strain distribution (strain gradient) both inside the thin film and the underlying substrate. Film force, F_f, ($F_f = t_f \times \bar{\sigma}$, where $\bar{\sigma}$ is the average film stress and t_f is the film thickness), was used to quantify the applied force onto the PMN-PT substrate. By convention, positive values are assigned to tensile film forces and negative values to compressive forces. Details for the measurement of film force are shown in Appendix A. Figure 1(h) shows a typical strain distribution inside the PMN-PT substrate underneath a metal strip with tensile film stress obtained by our FEA. Thus, by using the metal thin film strain gauges, we were able to introduce nonuniform strain distribution (strain gradient) inside the ferroelectric crystal and measure the corresponding converse piezoelectric strain response at the same time.

III. RESULTS AND DISCUSSION

A. Strain response with respect to film stress

To vary the film stress while keeping a same interface between the metal thin film and PMN-PT substrate, we fabricated strain gauges made by 50 nm Ag thin film and by 50 nm Cr thin film on top of 25 nm Ag thin film (Ag-Cr bilayer film). Here, silver, as a low melting point metal with high surface mobility, exhibited low tensile film stress, whereas chromium, as a high melting point metal with low surface mobility, exhibited high tensile film stress[43,44]. The film force for the silver alone film was measured to be at 3.6 N m^{-1} and the film force for the

Ag-Cr bilayer film was measured to be at 27.8 N m^{-1}. Since silver is more conductive than chromium (the resistance of the 25nm Ag layer was measured to be around 200 Ω, whereas the resistance of the 50nm Cr layer was measured to be around 1600 Ω), current mostly flows through the Ag layer, which makes both the silver-alone and the Ag-Cr bilayer film strain gauges having similar gauge factors (7.7 and 7.1, respectively). Figure 2(a) shows a typical IP strain response of the PMN-PT under the silver-alone strain gauge, which is non-volatile and unipolar with a left-hand polarity (shows high remanent strain after applying a negative gate voltage), similar as the strain response of Fig. 1(c). Figure 2(b) shows a typical IP strain response of the PMN-PT under the Ag-Cr bilayer film strain gauge, which is also non-volatile and unipolar, but with a right-hand polarity (shows high remanent strain after applying a positive gate voltage), similar as the strain response of Fig. 1(d). Similar results as in Fig. 2(a) and Fig. 2(b) have been confirmed by 15 silver-alone strain gauges and 10 Ag-Cr bilayer strain gauges on various PMN-PT substrates containing the same intrinsic internal bias field (PMN-PT crystals cut from same batch). The qualitative explanations for the opposite strain responses are given in Fig. 2(c) and Fig. 2(d), respectively. For the silver alone strain gauges with low film force, the nonuniform strain in the PMN-PT underneath the metal strip is small, thus the flexoelectric effect induced internal bias is trivially small. The left-hand unipolar non-volatile strain is caused by the positive **intrinsic** internal bias of the PMN-PT substrate, as shown in Fig. 2(c). Intrinsic internal bias has been widely observed in ferroelectric single crystals in their as-grown state, which can result from defect dipole alignment during the crystal growth process[5,45,46]. However, for the Ag-Cr bilayer film strain gauges with high film force, the nonuniform strain in the PMN-PT is large. This causes a strong negative flexoelectric internal bias which surpasses the positive intrinsic internal bias, thus resulting in the unipolar non-volatile strain response with opposite polarity, as shown in Fig. 2(d). It is worth mentioning that the results observed here cannot be explained by the bias field caused by the asymmetric bottom and top electrodes as silver is the contact material with PMN-PT for the top electrode in both

cases, and more generally, the work function difference between the top and bottom electrode is in the order of 1V whereas we are applying 150V gate voltage across the bulk PMN-PT single crystal. The results also cannot be explained by the change of the charge screening efficiency in the silver-PMN-PT interface, since the thicknesses of the metal thin films we used are well above the typical charge screening length for simple metals, which is on the order of an angstrom[47].

To further investigate the transition of the strain response from the left-hand unipolar curve to the right-hand unipolar curve, we gradually increased the applied film force to evaluate how the strain response would change correspondingly. To do this, we deposited different thickness of nickel on top of 25 nm silver (Ag-Ni bilayer film). As the melting point of Ni is higher than silver and lower than chromium, the average film stress $\bar{\sigma}$ of evaporated Ni thin films are also in between evaporated Ag thin films and Cr thin films[48]. Therefore, by gradually increasing the thickness of the evaporated Ni layer, we were able to control the film force F_f ($F_f = t_f \times \bar{\sigma}$) of the Ag-Ni bilayer film to increase from a film force close to Ag-alone film to a film force close to the Ag-Cr bilayer film, as shown in Fig. 3(a). Based on this, we fabricated Ag-Ni bilayer film strain gauges made from 25 nm, 40 nm, 55 nm, and 70 nm Ni on top of 25 nm Ag, which were measured to result in a film force of 8.1 N m^{-1}, 13.0 N m^{-1}, 18.6 N m^{-1}, and 22.5 N m^{-1}, respectively. Again, since silver is more conductive than nickel (the resistance of 25~70nm Ni layer was measured to be in the range of 600~1600 Ω), current mostly flows through the Ag layer (3 to 8 times). Figures 3(b)-(e) show the corresponding IP strain responses of the PMN-PT measured from these strain gauges. As the film force increases from left to right, a gradual transform from left-hand unipolar non-volatile curve [Fig. 3(b)] to the right-hand unipolar non-volatile curve [Fig. 3(e)] can be seen, with a bipolar volatile curve in between [Fig. 3(c)], which indicates that the positive intrinsic internal bias of the PMN-PT substrate was gradually overcome by the negative internal bias induced from the flexoelectric effect. The strain responses we measured from the three kinds of strain gauges (Ag-alone, Ag-

Cr bilayer, Ag-Ni bilayer) in Fig. 2 and Fig. 3 are comparable because the Ag is always the layer in contact (same interface between the strain gauges and the PMN-PT substrate), and the current always mostly flows through the Ag layer. The similar shape of the strain responses from Fig. 2(b) and Fig. 3(e) also verified that this effect is not because of the composition of the strain gauges, but mainly due to the film force of the strain gauges. Within these sets of experiments it is demonstrated that we have continuous engineerable control over ferroelastic non-volatility in our devices.

B. Modeling of the flexoelectric effect

To quantify the flexoelectric effect, we performed finite element analysis (FEA) of the strain distribution in the PMN-PT induced by the Ag-Cr bilayer film stressor consisting of 50nm Cr on top of 25nm Ag. The FEA methods used here have a long-standing history in process simulation for strained commercial silicon-based transistors and have been used exclusively to model strain in Si since the inception of strain engineering as a concept. We seek to use these same methods to understand strain gradients in our ferroelectrics, while later reconfirming with local experimental probes (section C). Here, the Ag/PMN-PT interface is described by a surface-based cohesive law with linear traction-separation behavior in the FEA model and characterized by a constant interfacial shear modulus G_{int}. This was necessary to model imperfect bonding/adhesion at the Ag and PMN-PT interface and represents the interface as a more compliant layer in between the two constituting materials, typical for systems of thin film metals on oxides. The value of G_{int} was determined to be at 3.6 GPa through the density functional theory (DFT) calculation and compared with other previously reported interfacial shear modulus of various metal/dielectric interfaces in Appendix B (Table I). Due to the high length-to-width ratio of the strips, the strain components corresponding to the length direction would be nearly uniform at any location along the strips. Consequently, those strain gradients and their contribution to flexoelectric polarization would be orders of magnitude smaller.

9

Hence, the plane-strain assumption was used in FEA to model the strain distribution in the $\vec{x}_2\vec{x}_3$-plane [same coordinates as in Fig. 1(e) and Fig. 1(f)]. The details of the FEA and DFT simulation can be found in Appendix C.

Figures 4(a)-(c) show the simulated strain distributions inside the PMN-PT underneath the Ag-Cr bilayer film, where ε_{22} and ε_{33} describe the normal strain in the IP ($\vec{x}_2$) and the OP ($\vec{x}_3$) direction, respectively, and ε_{23} describes the shear strain in the $\vec{x}_2\vec{x}_3$-plane. As shown in Fig. 4(a) and Fig. 4(b), there are large strain gradients formed inside the PMN-PT underneath the stressor layers near the surface region (~1µm in depth). It is important to note that the normal strain ε_{22} and ε_{33} shown in Fig. 4(a), (b) are axially symmetric, while the shear strain ε_{23} shown in Fig. 4(c) was antisymmetric across the strip. Based on the simulated strain distribution results in Fig. 4(a)-(c), we calculated the corresponding flexoelectric field near the surface of the PMN-PT (1µm in depth) with the details of the calculation described in Appendix C. As shown in Fig. 4(d), the average magnitude of the flexoelectric field close to the surface of the PMN-PT underneath the strip is around 2.6 kV cm^{-1}, which is 1 kV cm^{-1} higher than the coercive field of PMN-PT (~1.6 kV cm^{-1})[25]. The direction of the flexoelectric field in the OP direction is pointing downward, thus causing a strong negative internal bias in the PMN-PT. This matches with the prediction in Fig. 2(d). Moreover, the FEA results also reveal the unique asymmetry resulting from the effect of the antisymmetric shear strain ε_{23} on the flexoelectric field in the IP direction ($\vec{x}_2$). Under the strip, $\vec{E}_{flexo}$ is pointing to the right ([001]) for the left portion whereas $\vec{E}_{flexo}$ is pointing to the left ([00$\bar{1}$]) for the right portion, with the former region slightly **wider** than the latter, as marked by the black dashed line. This asymmetry could only arise due to the shear component of the flexoelectric effect, and will later be experimentally probed for as further evidence for flexoelectric induced internal bias modification. Additionally, as we traverse from left to right in the entire modelled region of the ferroelectric substrate, we see that

the IP domain configuration due to the flexoelectric field should have a "left-right-left-right" configuration, which will also be probed for experimentally as verification of our simulation.

C. Verification of modeling results by Piezoresponse Force Microscopy (PFM)

PFM is a well-known method used to map the surface domains in ferroelectrics, which can sense surface domains up to ~1µm in depth[49]. This depth resolution matches with the length scale of the flexoelectric field predicted in Fig. 4. Furthermore, according to the modeling results (section B), the flexoelectric field will result in a unique surface domain configuration in the PMN-PT along the IP direction. Therefore, we used PFM to systematically investigate the surface domain patterns of the PMN-PT substrate after the electrical measurements of the strain gauges to serve as further verification of the FEA model. We chose the Ag-Cr bilayer film strain gauges as they showed the strongest right-hand non-volatile unipolar strain response resulted from the flexoelectric effect. Figure 5(a) shows a typical Ag-Cr bilayer film strain gauge and the corresponding strain response. The poling sequence of the last electric-field sweeping were 0 kV cm^{-1} → +6 kV cm^{-1} → 0 kV cm^{-1} → -6 kV cm^{-1} → 0 kV cm^{-1} between the bottom electrode and the strain gauge. With the right-hand polarity of the strain response, the part of the PMN-PT substrate underneath the metal strip was therefore left at the low remanent strain state, which corresponds to the domain states with downward OP polarizations. The strain gauges were then removed by a relief polishing process with details described in Appendix A. Since domains with downward polarizations have a lower abrasion rate than ones with upward polarizations[50], the surface domain structures were revealed after the relief polishing. Multiple works have already demonstrated that through relief polishing, the topographic image will show the ferroelectric domain structure without changing the domain orientation itself[50-54]. As shown in Fig. 5(b), the region that used to be underneath the strain gauge with downward polarizations appeared to be smooth and higher than the surrounding regions, whereas the region far away from the former appeared to be uneven with mottled

pattern[50] because of the annealing process before the device fabrication which set the polarizations pointing randomly along the eight possible <111> directions. This also shows that the built-in intrinsic internal bias field is not large enough to re-orient the polarizations in the PMN-PT by itself.

PFM measurements were then immediately conducted over an area that covers both the region that used to be underneath the metal strip and the regions next to it in less than an hour after the removal of the stressor layers. It has already been demonstrated by multiple works that the domain patterns set by the flexoelectric effect is relatively stable and show no relaxation for over 12 hours to several days after the removal of the applied force that induced the flexoelectric field[35,38,55]. To uniquely identify the polarization direction for each domain, we performed one vertical (V) PFM [Fig. 5(c)] and two lateral (L) PFMs with the AFM probe along [001] [Fig. 5(d)] and [$\bar{1}$10] [Fig. 5(e)] respectively, where the VPFM can image the OP polarization component and the LPFM can image IP component perpendicular to the AFM probe. Figure 5(c) shows the VPFM phase image. Here, the measurement is sensitive to polarizations with an OP component, which are represented by the four polarization vectors in Fig. 5(f). Thus, the dark region indicates downward polarizations with two possible variants [marked as the blue and purple vectors at the bottom of Fig. 5(c) and in Fig. 5(f)] whereas the bright region indicates upward polarizations with the other two possible variants [marked as green and yellow vectors at the bottom of Fig. 5(c) and in Fig. 5(f)]. Figure 5(d) shows the LPFM phase image with the AFM probe along [001]. Here, the measurement is sensitive to polarizations which have an IP component perpendicular to [001], which are represented by the four polarization vectors in Fig. 5(g). However, no contrast was seen in Fig. 5(d), which indicates that there are no IP polarizations in the scanned area. Figure 5(e) shows the LPFM phase image with the AFM probe along [$\bar{1}$10]. This time, the measurement is sensitive to polarizations which have an IP component perpendicular to [$\bar{1}$10]. Although all 8 polarization directions along <111> have IP component perpendicular to [$\bar{1}$10], with the result from Fig. 5(d), we can eliminate 4 variants.

Only the vectors shown in Fig. 5(h) may cause contrast in Fig. 5(e). Therefore, by combining all three PFM results, the polarization direction for each domain can be uniquely identified, as marked at the bottom of Fig. 5(e). Here, the OP directions of the measured domains are the combined results determined from the applied external electric field, intrinsic internal bias field and the flexoelectric field, whereas the IP directions of the domains are solely determined from the flexoelectric field, which perfectly matches the "left-right-left-right" configuration that was modeled for the flexoelectric field [Fig. 4(d)]. Moreover, the **asymmetry** of the polarization in the IP direction of the PMN-PT underneath the strip predicted in Fig. 4(d) was also observed in the PFM result in Fig. 5(e), where the brighter region between the two red dashed lines is slightly wider than the darker region between the two red dashed lines. This effect has been reproduced in multiple regions of the strain gauge presented in Fig. 5, as well as other separate strain gauges with other film force magnitudes. This asymmetry exactly matching our FEA simulations, which has no free parameters in its model, provides further direct confirmation that the effects we observe in the control of non-volatile strain arise from flexoelectric induced internal bias modifications to the surface of the PMN-PT. It is worth mentioning at this point that all the methods we introduce here are surface sensitive effects, since the flexoelectric effects are limited to the surface (~1µm in depth) of the PMN-PT substrate. The gauges only measure strain applied by the domains directly underneath itself at the surface, while PFM only probes surface polarizations (~1µm in depth) of the PMN-PT single crystal. Direct polarization vs. electric-field measurements would likely not elicit the same effect since our PMN-PT substrates were 0.25 mm in thickness, whereas it is likely that in thin film ferroelectrics there could be a directly measurable effect, which can be done by using the recently reported ferroelectric membranes that are free from substrate clamping[56-58].

IV. CONCLUSION

We introduced another approach to induce flexoelectric effect in ferroelectric materials, by which controllable internal bias and polarity-reversibility of non-volatile ferroelastic strain can be achieved. This method is unique from flexoelectric control in the past since it uses techniques that have device-by-device continuous control of strain that have long been used in commercial fabrication processes in densely integrated and aggressively scaled transistor technology. Flexoelectricity was verified through process simulation with FEA using a model with **no free parameters**, which exactly matches the expected magnitude for flexoelectric field, directionality of flexoelectric polarization, and shear flexoelectric asymmetry. This provides a path to realize non-volatile control of strain sensitive materials properties (resistivity, band gap, magnetization, ferromagnetic resonance, superconductivity …) in deposited thin films and 2D materials in ferroelastic-strain based (straintronic) devices[17-23]. In fact, in many previously reported works on magnetic thin films on PMN-PT, there is always a small degree of straintronic non-volatility associated with asymmetry with respect to electric-field sweeping that may be due to unaccounted for strain-induced flexoelectric effects. With our learned knowledge and the ability to engineer the polarity of strain non-volatility, both PMOS-like and NMOS-like non-volatile straintronic devices may potentially be explored using the same base material as a channel, which is difficult to obtain by using ferroelectric field effect alone[40]. The ability to control internal bias also benefits the ferroelectric field-effect based electronic devices by adding another degree of freedom in those applications, especially in engineering new classes of ultrathin scalable ferroelectrics such as $Hf_{0.8}Zr_{0.2}O_2$ (HZO) with CMOS compatibility[39,40]. By adapting a long-existing technique from the semiconductor industry, i.e., stressed capping layer-based strain engineering[31-33], the thin film stress-induced flexoelectric effect we demonstrated here may lead to scalable method to control non-volatile FeFETs or straintronic devices.

ACKNOWLEDGEMENTS

APPENDIX A: EXPERIMENTAL DETAILS

PMN-PT substrate preparation

(110)-oriented PMN-PT single-crystals (0.25 mm in thickness) with e-beam deposited Cu(100 nm) top electrode and sputtered Au(100 nm)/Ti(5 nm) bottom electrode were prepoled under an electric field of $6\,\mathrm{kV\,cm^{-1}}$ across the top and bottom surface. After prepoling, the top surface was first polished using diamond lapping film with 1 μm grit for 2 min to remove the top Cu electrode and then polished by poromeric polishing pads with colloidal silica suspension of (~60 nm) abrasive particles for 15 min to get the average roughness (R_a) ~0.5 nm. After polishing, the PMN-PT substrates were annealed at 125 °C for 30 min to set the polarizations in the crystal pointing randomly. We found this step critical to ensure consistent strain responses from PMN-PT under each film forces and to preserve the domain configurations against ferroelastic relaxation which could re-orient the polarizations[59,60] underneath the strain gauges after the relief polishing. The R_a after the annealing was below 0.8 nm.

Device fabrication

After the preparation of the PMN-PT substrate, metal thin film strain gauges were patterned using a lift-off process onto the top surface along the [$\bar{1}$10] direction by direct-write laser photolithography using a Microtech LW405 laserwriter system and S1805 photoresist. All metals were deposited using e-beam evaporation under a chamber pressure between 1×10^{-5} torr and 3×10^{-5} torr at a rate of 1 Å s^{-1}. For strain gauges consist of different metal films, the vacuum condition was maintained throughout the whole deposition process.

Device characterization

Resistance of the strain gauges were measured at room temperature using low frequency a.c. lock-in techniques (3 Hz) with the a.c. voltage signal provided by a separated phase-locked function generator. The poling electric fields were applied through gate voltages between the bottom electrode and the strain gauge using a d.c. power supply and were typically applied for 6 s before each resistance measurement. For all strain gauges, the poling electric fields were cycled between -6 kV cm^{-1} and +6 kV cm^{-1} with a step of 0.2 kV cm^{-1} for 6 times to confirm the repeatability of the results.

Film force characterization

Metal thin films were deposited onto cleaned coverslips using the same evaporation conditions as the fabrication of the strain gauges. The radius of curvature of the coverslips before (r_0) and after (r) the deposition were measured using the contact profilometry. The average film stress, $\bar{\sigma}$, was quantified using the Stoney equation[61,62], $\bar{\sigma} = \frac{-E_s \times t_s^2}{6 \times (1-v_s) \times t_f} \times (\frac{1}{r} - \frac{1}{r_0})$, where E_s, v_s, and t_s are the Young's modulus, Poisson's ratio and the thickness of the cover slip, respectively, t_f is the thickness of the thin film. The applied film force, F_f, i.e., force per unit width, can then be calculated through $F_f = t_f \times \bar{\sigma}$.

Strain gauge calibration

The same strain gauges fabricated on the PMN-PT substrates were deposited on flexible Kapton substrates. By applying various amount of strain through bending the Kapton substrate and measuring the corresponding resistance changes of the strain gauge, the gauge factor was calibrated through the equation $GF = \frac{\Delta R/R}{\varepsilon}$,where ε is the applied strain, R is resistance of the strain gauge, GF is the gauge factor. Here, the value of strain ε was deduced from $\varepsilon = t_k/2r_k$, where $t_k = 127$ μm is the thickness of the Kapton substrate and r_k is the radius of curvature of the bent substrate[16]. The gauge factor for the Ag-alone, Ag-Cr bilayer, Ag-Ni bilayer strain gauge was measured to be 7.7, 7.1, 5.1, respectively.

Relief polishing

The domains underneath the Ag-Cr bilayer strain gauges were left at the low remanent strain state after the electric-field cycling. The relief polishing process was then conducted as follows. The top surface of the PMN-PT substrate was first polished on a poromeric polishing pad with colloidal silica suspension of (~60nm) abrasive particles for 30 s to remove the strain gauges. This was found to be long enough to remove the metal thin film strain gauges while short enough to preserve the domains nanometers below the sample surface, as the abrasion rates of materials with colloidal silica are typically around 40-120 nm min^{-1}[63]. After that, the surface was polished on another clean poromeric polishing pad with water rinse turned on for 2 minutes to clean off the residue polishing media on the PMN-PT surface.

Piezoresponse force microscopy

PFM was performed on an atomic force microscope (Solver NEXT) from NT-MDT using conductive AFM probes (PPP-NCHPt) from NANOSENSORS with a typical voltage of V_{ac} = 1 V and frequency of 125 kHz between the tip and the bottom electrode of the PMN-PT under ambient conditions at room temperature. To uniquely identify the polarization direction for each domain, VPFM and LPFM were first conducted when the AFM probe was along [001]. After that, the sample was rotated by 90 ° so that the AFM probe was along [$\bar{1}$10]. LPFM were then conducted again on the same region. By this way, the components along all three possible Cartesian directions for each polarization were measured.

APPENDIX B: COMPARISON OF INTERFACIAL SHEAR MODULUS OF VARIOUS INTERFACES

Comparison of the interfacial shear modulus G_{int} of similar systems from previously reported studies is listed in Table I. It can be observed that the average interfacial shear modulus varies from as low as ~2 GPa to higher values like ~70 GPa. This value depends on the crystal structure of the two materials and coherency of the stacked layers. Our system, which has two materials with different crystal structures, experiences some stacking incoherency at the interface. Thus,

we obtained a slightly lower value of interfacial shear modulus at Ag/PMN-PT interface. The deduced G_{int} value from the DFT calculation falls within the range of the interfacial shear modulus values for similar reported systems and hence we have used it further for modeling flexoelectric field distribution results in FEA.

TABLE I. Comparison of the interfacial shear modulus of similar metal/dielectric interfaces from the literature

System	Interfacial shear modulus [GPa]
Ag/PMN-PT (this work)	3.6
Cu/TiN[64]	2.68*
Ti/TiN[65]	3.08*
Ni/Al$_2$O$_3$[66]	5.13*
Ag/MgO[67]	9.35
Al/TiN[64]	12.1*
Ni/ZrO$_2$[68]	31.3
Al/Al$_2$O$_3$[69]	59.6
Al/SiC[70]	70.2

Calculated based on the reported values of ideal shear strength and lattice geometry of the system.

APPENDIX C: MODELING DETAILS

DFT simulation of the interfacial shear modulus

We have performed DFT simulations to calculate the interfacial shear modulus at the interface of Ag and PMN-PT. All the calculations were performed using the Atomistix Toolkit (QuntumATK) commercial package. The self-consistent calculations were carried out with Perdew–Burke–Ernzerhof (PBE) exchange–correlation functional within the Generalized Gradient Approximation (GGA)[71,72]. The projector augmented wave (PAW) method[73] was applied with a plane wave cutoff of 400 eV for parametrization of the exchange-correlation functional. An energy convergence criterion of 10^{-5} eV is considered for each self-consistent cycle. For simplicity, PMN-PT crystal has been modelled as Pb(Mg$_{1/3}$Nb$_{2/3}$)O$_3$ (PMN) structure. Similar to what reported by Suewattana et al[74] and Kiguchi et al[75], the modeled system

consists of a 15-atom cell with $1 \times 1 \times 3$ super-lattice having 1:2 ordering of Mg and Nb. Bulk Ag, which has a face-centered cubic (FCC) structure is stacked on top of PMN-PT crystal surface. To build the Ag/PMN interface, we stacked the PMN and Ag layers in a similar way demonstrated by Oleinik et al[76]. The entire system is relaxed using conjugate gradient (CG) algorithm until the total atomic forces are smaller than cut-off threshold of 0.01 eV Å^{-1}. To integrate the Brillouin zone, a $10 \times 10 \times 1$ k-point mesh is used using the Monkhorst-Pack scheme[77]. Same as previous works[64,66,67], to obtain the interfacial shear modulus (G_{int}) at the Ag/PMN interface, the Ag layers were displaced over the PMN surface and G_{int} was derived from the interlayer binding energy (E_b). E_b is obtained as $E_b = E_{Ag/PMN} - E_{Ag} - E_{PMN}$, where $E_{Ag/PMN}$ is the energy of the optimized combined system and E_{Ag} and E_{PMN} the energies of the individual optimized Ag and PMN layers. Taking the first order derivative of E_b, we obtain the shear force (F_s) experienced in the sliding direction. And the shear stress, t_t, can be obtained as $t_t = F_s/A$, where A is the area at the Ag/PMN interface. Finally, the interfacial shear modulus is calculated as $G_{int} = t_t/\varepsilon_t$, where ε_t is the shear strain applied on displacing the Ag layers. Also, since Ag is a polycrystalline material, we have considered different orientations of Ag layers by rotating them over PMN surface and thus, calculated shear modulus in different directions. We have then obtained the average interfacial shear modulus (3.6 GPa) incorporating all considered orientations.

FEA simulation of the strain distribution

To model the strain gradient and the resultant flexoelectric field distributions in the PMN-PT under the application of stress from the metal thin films, FEA was conducted using ABAQUS, a commercially available program. The metal films and PMN-PT substrates were modeled in plane strain condition (as the length of the metal strip is ~50 times larger than the width in our fabricated devices) with eight-node quadratic plane strain (CPE8) elements. All the materials were taken to be isotropic and linear elastic with their Young's modulus being 279, 83, and 20

GPa[78,79] with Poisson's ratio of 0.21,0.37, and 0.3 for Cr, Ag, and PMN-PT, respectively. The width of both metal films was set to 10μm with their thickness taken to be 50 nm and 25 nm respectively for the Cr and Ag layer. The PMN-PT substrate was 30 μm wide with a thickness of 10 μm. A fine mesh size of 20 nm was created in the substrate which resulted in a total of 750,000 elements to provide a fine resolution for calculations of strain gradients. In addition, dimensions and mesh size were selected such that the strain field underneath the metal-substrate interface reached convergence and was unaffected by the geometry of edges.

The behavior of the Ag/PMN-PT interface was described by a cohesive zone model (CZM) with a linear traction-separation law already implemented in ABAQUS. In this way, the interface can be made relatively compliant (lower stiffness) than the two constituting elastic bodies as observed from the DFT simulations. Traction-separation law can be surface-based in ABAQUS where the stiffness is defined as an interaction property, or element based where it is defined as a material property although the constitutive relations are almost the same for both descriptions. The constitutive relationship for 2D cohesive elements can be written as follows[80]:

$$T = \begin{pmatrix} t_n \\ t_t \end{pmatrix} = \begin{bmatrix} k_{nn} & k_{nt} \\ k_{nt} & k_{tt} \end{bmatrix} \begin{pmatrix} \varepsilon_n \\ \varepsilon_t \end{pmatrix} = K\varepsilon \qquad (1)$$

here, t_n and t_t are the traction stress components in the normal and shear direction respectively with K being the nominal cohesive stiffness matrix of the interface, ε_n and ε_t are the corresponding nominal strain components. For the uncoupled linear traction separation behavior (ε_t does not give rise to stress in normal direction and vice versa), the off-diagonal terms can be set to zero and the constitutive response then becomes:

$$T = \begin{pmatrix} t_n \\ t_t \end{pmatrix} = \begin{bmatrix} k_{nn} & 0 \\ 0 & k_{tt} \end{bmatrix} \begin{pmatrix} \varepsilon_n \\ \varepsilon_t \end{pmatrix} = K\varepsilon \qquad (2)$$

We set the stiffness matrix element k_{tt} in equation (2) equal to G_{int} from our DFT calculation.

Now, the nominal strains in equation (2) are defined as following: $\varepsilon_n = \frac{\delta_n}{T_o}$, $\varepsilon_t = \frac{\delta_t}{T_o}$, where δ_n

is the normal separation (debonding) and δ_t is the shear separation (slippage) across the interface, T_o is the constitutive thickness of the cohesive element. If the value of T_o is taken to be 1.0, then the nominal strains in equation (2) become equal to the corresponding separations. As a result, the constitutive relationship can be equivalently written as:

$$T = \begin{pmatrix} t_n \\ t_t \end{pmatrix} = \begin{bmatrix} k_{nn} & 0 \\ 0 & k_{tt} \end{bmatrix} \begin{pmatrix} \delta_n \\ \delta_t \end{pmatrix} = K\delta \qquad (3)$$

which is the traction-separation constitutive law for surface-based cohesive model in ABAQUS. In this work, we used the surface-based linear elastic cohesive zone model along with the assumption that no damage occurs at the interface.

As the applied tensile film stress is expected to transfer from the metal to substrate by interfacial shear stress, and no normal debonding is observed, only shear traction-separation law was assumed in the cohesive model, i.e., $k_{nn} = 0$ in equation (3). In surface based cohesive model, interface slippage δ_t is defined as the contact separation which is the relative displacements between the nodes on one surface (PMN-PT) and their corresponding projection points on the other contacting (Ag) surface along the contact (interface) shear direction. Concepts of strain and displacement are reinterpreted as contact separations as mentioned earlier. The cohesive model represents the interface by an equivalent spring connecting the two elastic bodies (metal film and PMN-PT). Similar cohesive law has been previously used for describing many different types of interfaces[81-84].

We set the magnitude of the shear stiffness parameter in FEA model same as the average G_{int} obtained from our DFT simulations. Furthermore, the choice of this model parameter best reproduced experimental observations. A comparison with the results from stiffer (no slippage) as well as more compliant (smaller G_{int}, strong slippage) interfaces that may be possible from different relative orientation of two crystals are also presented as an additional validation in Appendix D (Fig. 6). Biaxial tensile stress of 966 MPa and 60 MPa (taken from experimental measurements) were applied on the Cr and Ag film respectively with imposing a fixed boundary

condition at the bottom of the PMN-PT along the thickness direction while keeping its edges free. Both normal and shear strain components at every elemental node were used from the FEA models to numerically calculate the corresponding strain gradients.

Calculation of flexoelectric field

Flexoelectric polarization is given by: $P_l = \mu_{ijkl}\frac{\partial \varepsilon_{kl}}{\partial x_j}$[28,29], where μ_{ijkl} is the flexoelectric tensor, ε_{kl} is the strain and x_j is the spatial coordinates. For PMN-PT with rhombohedral symmetry, μ_{ijkl} has 18 independent components[85]. However, full flexoelectric tensor components for PMN-PT have never been calculated theoretically and extracting all coefficients from experiment is challenging. In fact, only effective transverse flexoelectric coefficient μ_{13}^{eff} for (100)-oriented PMN-PT has been measured experimentally, with a value in the range of 10-70 µC cm^{-1} at room temperature[41,42]. To make an estimation of each tensor component, we assumed cubic symmetry of PMN-PT and took $\mu_{1111}= \mu_{2222}= \mu_{3333}= \mu_{11}= 1$ µC cm^{-1} , $\mu_{1122}= \mu_{1133}= \mu_{2211}=\mu_{2233}= \mu_{3311}= \mu_{3322}= \mu_{12}= 16$ µC cm^{-1}, $\mu_{1221}= \mu_{1331}= \mu_{2112}=\mu_{2332}= \mu_{3112}= \mu_{3223}= \mu_{44} = 1$ µC cm^{-1} for (100)-oriented PMN-PT. Based on the equation, $\mu_{13}^{eff} = \frac{-c_{12}}{c_{11}+c_{12}}\mu_{11} + \frac{c_{11}}{c_{11}+c_{12}}\mu_{12}$[86,87], where c_{11} and c_{12} are the elastic stiffness tensor components of PMN-PT[78], the estimated tensor values yield an effective transverse flexoelectric coefficient around 10 µC cm^{-1}, which is within the range of the experimental value. For (110)-oriented PMN-PT, as the coordinates are rotated from where $\hat{x}_1, \hat{x}_2$ and $\hat{x}_3$ along [001], [010] and [100], respectively, to along [$\bar{1}10$], [001] and [110], respectively, the flexoelectric coefficients therefore transform to $\mu'_{33} = \frac{\mu_{11}+\mu_{12}+2\mu_{44}}{2}= 9.5$ µC cm^{-1}, $\mu'_{22} = \mu_{11}= 1$ µC cm^{-1}, $\mu'_{23} = \mu'_{32} = \mu_{12} = 16$ µC cm^{-1}, $\mu'_{44} = \mu_{44} = 1$ µC cm^{-1}[86]. Under the assumption of plane strain, only strain ε_{22}, ε_{33}, and ε_{23} are considered. Flexoelectric polarization, $\vec{P}(0, P_2, P_3)$, can therefore be calculated by $P_2 = \mu'_{22}\frac{\partial \varepsilon_{22}}{\partial x_2} + \mu'_{23}\frac{\partial \varepsilon_{33}}{\partial x_2} + \mu'_{44}\frac{\partial \varepsilon_{23}}{\partial x_3}$, $P_3 = \mu'_{33}\frac{\partial \varepsilon_{33}}{\partial x_3} + \mu'_{32}\frac{\partial \varepsilon_{22}}{\partial x_3} + \mu'_{44}\frac{\partial \varepsilon_{23}}{\partial x_2}$ [88], where the strain gradients were obtained from the FEA

model. Flexoelectric field, $\vec{E}_{flexo}$, was derived from the flexoelectric polarization by $\vec{E}_{flexo} = \frac{\vec{P}}{\varepsilon_0 \varepsilon_r}$, where ε_0 is the permittivity of vacuum and $\varepsilon_r = 1800$ for PMN-PT[78].

APPENDIX D: COMPARISON OF THE SIMULATED FLEXOELECTRIC FIELD BASED ON DIFFERENT VALUES OF G_{int}

Simulated flexoelectric fields inside the PMN-PT underneath the Ag-Cr bilayer film based on different values of G_{int} are shown in Fig. 6, where G_{int} increases from a strong slippage condition ($G_{int} = 0.5$ GPa) to the no slippage condition. As shown in Fig. 6, when the value of G_{int} is at 3.6 GPa, the magnitude of E_{flexo} near the surface of the PMN-PT underneath the strip is above 2 kV cm^{-1}, whereas in both the strong slippage and the no slippage condition, the magnitude of E_{flexo} near the surface of the PMN-PT underneath the strip decreases to below half of the coercive field of PMN-PT (< 0.8 kV cm^{-1}).

Reference

[1]   J. F. Scott and C. A. P. Dearaujo, Ferroelectric Memories, Science **246**, 1400 (1989).

[2]   S. Mathews, R. Ramesh, T. Venkatesan, and J. Benedetto, Ferroelectric field effect transistor based on epitaxial perovskite heterostructures, Science **276**, 238 (1997).

[3]   P. Maksymovych, S. Jesse, P. Yu, R. Ramesh, A. P. Baddorf, and S. V. Kalinin, Polarization control of electron tunneling into ferroelectric surfaces, Science **324**, 1421 (2009).

[4]   V. Garcia, S. Fusil, K. Bouzehouane, S. Enouz-Vedrenne, N. D. Mathur, A. Barthelemy, and M. Bibes, Giant tunnel electroresistance for non-destructive readout of ferroelectric states, Nature **460**, 81 (2009).

[5]   G. Arlt and H. Neumann, Internal bias in ferroelectric ceramics: origin and time dependence, Ferroelectrics **87**, 109 (1988).

[6]   S. Wu, S. A. Cybart, D. Yi, J. M. Parker, R. Ramesh, and R. Dynes, Full electric control of exchange bias, Phys. Rev. Lett. **110**, 067202 (2013).

[7]   S. Wu, S. A. Cybart, P. Yu, M. Rossell, J. Zhang, R. Ramesh, and R. Dynes, Reversible electric control of exchange bias in a multiferroic field-effect device, Nat. Mater. **9**, 756 (2010).

[8]   A. R. Damodaran, E. Breckenfeld, Z. H. Chen, S. Lee, and L. W. Martin, Enhancement of Ferroelectric Curie Temperature in $BaTiO_3$ Films via Strain-Induced Defect Dipole Alignment, Adv. Mater. **26**, 6341 (2014).

[9]   S. Saremi, J. Kim, A. Ghosh, D. Meyers, and L. W. Martin, Defect-Induced (Dis)Order in Relaxor Ferroelectric Thin Films, Phys. Rev. Lett. **123** (2019).

[10]   D. Lee, B. C. Jeon, A. Yoon, Y. J. Shin, M. H. Lee, T. K. Song, S. D. Bu, M. Kim, J. S. Chung, J. G. Yoon *et al.*, Flexoelectric Control of Defect Formation in Ferroelectric Epitaxial Thin Films, Adv. Mater. **26**, 5005 (2014).

[11]   P. Yu, W. Luo, D. Yi, J. X. Zhang, M. D. Rossell, C. H. Yang, L. You, G. Singh-Bhalla, S. Y. Yang, Q. He *et al.*, Interface control of bulk ferroelectric polarization, Proc. Natl. Acad. Sci. U. S. A. **109**, 9710 (2012).

[12]   C. Lichtensteiger, S. Fernandez-Pena, C. Weymann, P. Zubko, and J. M. Triscone, Tuning of the Depolarization Field and Nanodomain Structure in Ferroelectric Thin Films, Nano Lett. **14**, 4205 (2014).

[13]   B. C. Jeon, D. Lee, M. H. Lee, S. M. Yang, S. C. Chae, T. K. Song, S. D. Bu, J. S. Chung, J. G. Yoon, and T. W. Noh, Flexoelectric Effect in the Reversal of Self-Polarization and Associated Changes in the Electronic Functional Properties of BiFeO3 Thin Films, Adv. Mater. **25**, 5643 (2013).

[14]   D. Lee, A. Yoon, S. Jang, J.-G. Yoon, J.-S. Chung, M. Kim, J. Scott, and T. W. Noh, Giant flexoelectric effect in ferroelectric epitaxial thin films, Phys. Rev. Lett. **107**, 057602 (2011).

[15]   A. M. Smith, A. M. Mohs, and S. Nie, Tuning the optical and electronic properties of colloidal nanocrystals by lattice strain, Nat. Nanotechnol. **4**, 56 (2009).

[16]   O. B. Aslan, I. M. Datye, M. J. Mleczko, K. Sze Cheung, S. Krylyuk, A. Bruma, I. Kalish, A. V. Davydov, E. Pop, and T. F. Heinz, Probing the Optical Properties and Strain-Tuning of Ultrathin $Mo_{1-x}W_xTe_2$, Nano Lett. **18**, 2485 (2018).

[17]   R. Cherifi, V. Ivanovskaya, L. Phillips, A. Zobelli, I. Infante, E. Jacquet, V. Garcia, S. Fusil, P. Briddon, and N. Guiblin, Electric-field control of magnetic order above room temperature, Nat. Mater. **13**, 345 (2014).

[18]   Y. Lee, Z. Liu, J. T. Heron, J. D. Clarkson, J. Hong, C. Ko, M. D. Biegalski, U. Aschauer, S.-L. Hsu, and M. E. Nowakowski, Large resistivity modulation in mixed-phase metallic systems, Nat. Commun. **6**, 5959 (2015).

[19]   S. Zhang, Y. G. Zhao, P. S. Li, J. J. Yang, S. Rizwan, J. X. Zhang, J. Seidel, T. L. Qu, Y. J. Yang, Z. L. Luo *et al.*, Electric-Field Control of Nonvolatile Magnetization in $Co_{40}Fe_{40}B_{20}/Pb(Mg_{1/3}Nb_{2/3})_{0.7}Ti_{0.3}O_3$ Structure at Room Temperature, Phys. Rev. Lett. **108**, 137203 (2012).

[20]   W. Zhou, C. Ma, Z. Gan, Z. Zhang, X. Wang, W. Tan, and D. Wang, Manipulation of anisotropic magnetoresistance and domain configuration in Co/PMN-PT (011) multiferroic heterostructures by electric field, Appl. Phys. Lett. **111**, 052401 (2017).

[21]   M. Liu, J. Hoffman, J. Wang, J. Zhang, B. Nelson-Cheeseman, and A. Bhattacharya, Non-volatile ferroelastic switching of the Verwey transition and resistivity of epitaxial Fe_3O_4/PMN-PT (011), Sci. Rep. **3**, 1876 (2013).

[22]   M. Liu, B. M. Howe, L. Grazulis, K. Mahalingam, T. X. Nan, N. X. Sun, and G. J. Brown, Voltage-Impulse-Induced Non-Volatile Ferroelastic Switching of Ferromagnetic Resonance for Reconfigurable Magnetoelectric Microwave Devices, Adv. Mater. **25**, 4886 (2013).

[23]   W. Hou, A. Azizimanesh, A. Sewaket, T. Pena, C. Watson, M. Liu, H. Askari, and S. M. Wu, Strain-based room-temperature non-volatile $MoTe_2$ ferroelectric phase change transistor, Nat. Nanotechnol. **14**, 668 (2019).

[24]   A. Chen, A review of emerging non-volatile memory (NVM) technologies and applications, Solid-State Electron. **125**, 25 (2016).

[25]   T. Wu, P. Zhao, M. Bao, A. Bur, J. L. Hockel, K. Wong, K. P. Mohanchandra, C. S. Lynch, and G. P. Carman, Domain engineered switchable strain states in ferroelectric (011)[Pb(Mg$_{1/3}$Nb$_{2/3}$)O$_3$]$_{(1-x)}$-[PbTiO$_3$]$_x$ (PMN-PT, x$\approx$ 0.32) single crystals, J. Appl. Phys. **109**, 124101 (2011).

[26]   D. Lupascu and J. Rödel, Fatigue in bulk lead zirconate titanate actuator materials, Adv. Eng. Mater. **7**, 882 (2005).

[27]   W. H. Liang, F. X. Hu, J. Zhang, H. Kuang, J. Li, J. F. Xiong, K. M. Qiao, J. Wang, J. R. Sun, and B. G. Shen, Anisotropic nonvolatile magnetization controlled by electric field in amorphous SmCo thin films grown on (011)-cut PMN-PT substrates, Nanoscale **11**, 246 (2019).

[28]   P. Zubko, G. Catalan, and A. K. Tagantsev, Flexoelectric effect in solids, Annu. Rev. Mater. Res. **43**, 387 (2013).

[29]   B. Wang, Y. Gu, S. Zhang, and L.-Q. Chen, Flexoelectricity in solids: Progress, challenges, and perspectives, Prog. Mater. Sci. **106**, 100570 (2019).

[30]   G. Tsutsui, S. Mochizuki, N. Loubet, S. W. Bedell, and D. K. Sadana, Strain engineering in functional materials, AIP Adv. **9**, 030701 (2019).

[31]   T. Acosta and S. Sood, Engineering strained silicon-looking back and into the future, IEEE Potentials **25**, 31 (2006).

[32]   S. E. Thompson, G. Sun, Y. S. Choi, and T. Nishida, Uniaxial-process-induced strained-Si: Extending the CMOS roadmap, IEEE Trans. Electron Devices **53**, 1010 (2006).

[33]   S. Orain, V. Fiori, D. Villanueva, A. Dray, and C. Ortolland, Method for managing the stress due to the strained nitride capping layer in MOS transistors, IEEE Trans. Electron Devices **54**, 814 (2007).

[34]   G. Catalan, A. Lubk, A. Vlooswijk, E. Snoeck, C. Magen, A. Janssens, G. Rispens, G. Rijnders, D. H. Blank, and B. Noheda, Flexoelectric rotation of polarization in ferroelectric thin films, Nat. Mater. **10**, 963 (2011).

[35]   H. Lu, C.-W. Bark, D. E. De Los Ojos, J. Alcala, C. B. Eom, G. Catalan, and A. Gruverman, Mechanical writing of ferroelectric polarization, Science **336**, 59 (2012).

[36]   J. Ocenasek, H. Lu, C. W. Bark, C. B. Eom, J. Alcala, G. Catalan, and A. Gruverman, Nanomechanics of flexoelectric switching, Phys. Rev. B **92**, 035417 (2015).

[37]   K. Cordero- Edwards, N. Domingo, A. Abdollahi, J. Sort, and G. Catalan, Ferroelectrics as smart mechanical materials, Adv. Mater. **29**, 1702210 (2017).

[38]   S. M. Park, B. Wang, S. Das, S. C. Chae, J. S. Chung, J. G. Yoon, L. Q. Chen, S. M. Yang, and T. W. Noh, Selective control of multiple ferroelectric switching pathways using a trailing flexoelectric field, Nat. Nanotechnol. **13**, 366 (2018).

[39]   S. S. Cheema, D. Kwon, N. Shanker, R. dos Reis, S. L. Hsu, J. Xiao, H. G. Zhang, R. Wagner, A. Datar, M. R. McCarter *et al.*, Enhanced ferroelectricity in ultrathin films grown directly on silicon, Nature **580**, 478 (2020).

[40]   A. I. Khan, A. Keshavarzi, and S. Datta, The future of ferroelectric field-effect transistor technology, Nat. Electron. **3**, 588 (2020).

[41]   J. Narvaez and G. Catalan, Origin of the enhanced flexoelectricity of relaxor ferroelectrics, Appl. Phys. Lett. **104**, 162903 (2014).

[42]   L. Shu, M. Wan, X. Jiang, F. Li, N. Zhou, W. Huang, and T. Wang, Frequency dispersion of flexoelectricity in PMN-PT single crystal, AIP Adv. **7**, 015010 (2017).

[43]   R. Koch, Stress in evaporated and sputtered thin films–a comparison, Surf. Coat. Technol. **204**, 1973 (2010).

[44]   R. Abermann and R. Koch, The internal stress in thin silver, copper and gold films, Thin Solid Films **129**, 71 (1985).

[45]   L. M. Zheng, L. Y. Yang, Y. R. Li, X. Y. Lu, D. Huo, W. M. Lu, R. Zhang, B. Yang, and W. W. Cao, Origin of Improvement in Mechanical Quality Factor in Acceptor-Doped Relaxor-Based Ferroelectric Single Crystals, Phys. Rev. Appl. **9**, 064028 (2018).

[46]   C. He, Z. J. Wang, X. Z. Li, X. M. Yang, X. F. Long, and Z. G. Ye, Self-polarized high piezoelectricity and its memory effect in ferroelectric single crystals, Acta Mater. **125**, 498 (2017).

[47]   M. Stengel, D. Vanderbilt, and N. A. Spaldin, Enhancement of ferroelectricity at metal-oxide interfaces, Nat. Mater. **8**, 392 (2009).

[48]   E. Klokholm and B. Berry, Intrinsic stress in evaporated metal films, J. Electrochem. Soc. **115**, 823 (1968).

[49]   F. Johann, Y. J. Ying, T. Jungk, Á. Hoffmann, C. L. Sones, R. W. Eason, S. Mailis, and E. Soergel, Depth resolution of piezoresponse force microscopy, Appl. Phys. Lett. **94**, 172904 (2009).

[50]   M. F. Wong and K. Zeng, Mechanical polishing effects toward surface domain evolution in $Pb(Zn_{1/3}Nb_{2/3})O_3$–$PbTiO_3$ single crystals, J. Am. Ceram. Soc. **94**, 1079 (2011).

[51]   A. R. Akhmatkhanov, E. D. Greshnyakov, A. D. Ushakov, E. M. Vaskina, D. O. Alikin, X. Wei, Z. Xu, Z. Li, S. Wang, Y. Zhuang *et al.*, Polarization reversal and domain kinetics in PMN-30PT single crystals, Ferroelectrics **508**, 31 (2017).

[52]   Q. Hu, A. D. Ushakov, A. A. Esin, E. O. Vlasov, D. S. Chezganov, L. Sun, A. P. Turygin, X. Wei, and V. Y. Shur, Investigation of domain structure evolution during zero-field temperature treatment in 0.67PMN-0.33PT single crystals, Ferroelectrics **525**, 114 (2018).

[53]   T. Scholz, B. Mihailova, G. A. Schneider, N. Pagels, J. Heck, T. Malcherek, R. P. Fernandes, V. Marinova, M. Gospodinov, and U. Bismayer, Ferroelectric properties of ruthenium-doped lead zinc niobate-lead titanate single crystal, J. Appl. Phys. **106**, 074108 (2009).

[54]   Q. Li, Y. Liu, R. L. Withers, Y. H. Wan, Z. R. Li, and Z. Xu, Piezoresponse force microscopy studies on the domain structures and local switching behavior of $Pb(In_{1/2}Nb_{1/2})O_3$-$Pb(Mg_{1/3}Nb_{2/3})O_3$-$PbTiO_3$ single crystals, J. Appl. Phys. **112** (2012).

[55]   A. Gruverman, B. J. Rodriguez, A. I. Kingon, R. J. Nemanich, A. K. Tagantsev, J. S. Cross, and M. Tsukada, Mechanical stress effect on imprint behavior of integrated ferroelectric capacitors, Appl. Phys. Lett. **83**, 728 (2003).

[56]   G. H. Dong, S. Z. Li, M. T. Yao, Z. Y. Zhou, Y. Q. Zhang, X. Han, Z. L. Luo, J. X. Yao, B. Peng, Z. Q. Hu *et al.*, Super-elastic ferroelectric single-crystal membrane with continuous electric dipole rotation, Science **366**, 475 (2019).

[57]   J. Irwin, S. Lindemann, W. Maeng, J. J. Wang, V. Vaithyanathan, J. M. Hu, L. Q. Chen, D. G. Schlom, C. B. Eom, and M. S. Rzchowski, Magnetoelectric Coupling by Piezoelectric Tensor Design, Sci. Rep. **9**, 19158 (2019).

[58]   H. S. Kum, H. Lee, S. Kim, S. Lindemann, W. Kong, K. Qiao, P. Chen, J. Irwin, J. H. Lee, S. E. Xie *et al.*, Heterogeneous integration of single-crystalline complex-oxide membranes, Nature **578**, 75 (2020).

[59]   M. P. Cruz, Y. H. Chu, J. X. Zhang, P. L. Yang, F. Zavaliche, Q. He, P. Shafer, L. Q. Chen, and R. Ramesh, Strain control of domain-wall stability in epitaxial $BiFeO_3$ (110) films, Phys. Rev. Lett. **99**, 217601 (2007).

[60]   S. H. Baek, H. W. Jang, C. M. Folkman, Y. L. Li, B. Winchester, J. X. Zhang, Q. He, Y. H. Chu, C. T. Nelson, M. S. Rzchowski *et al.*, Ferroelastic switching for nanoscale non-volatile magnetoelectric devices, Nat. Mater. **9**, 309 (2010).

[61]   J. S. Kim, K. W. Paik, and S. H. Oh, The multilayer-modified Stoney's formula for laminated polymer composites on a silicon substrate, J. Appl. Phys. **86**, 5474 (1999).

[62]   G. C. Janssen, M. Abdalla, F. Van Keulen, B. Pujada, and B. Van Venrooy, Celebrating the 100th anniversary of the Stoney equation for film stress: Developments from polycrystalline steel strips to single crystal silicon wafers, Thin Solid Films **517**, 1858 (2009).

[63]   Z. Zhang, W. Liu, and Z. Song, Effect of ammonium molybdate concentration on chemical mechanical polishing of glass substrate, J. Semicond. **31**, 116003 (2010).

[64]   S. K. Yadav, R. Ramprasad, J. Wang, A. Misra, and X. Y. Liu, First-principles study of Cu/TiN and Al/TiN interfaces: weak versus strong interfaces, Model. Simul. Mater. Sci. Eng. **22**, 035020 (2014).

[65]   X. M. Zhang, B. Zhang, Y. Mu, S. Shao, C. D. Wick, B. R. Ramachandran, and W. J. Meng, Mechanical failure of metal/ceramic interfacial regions under shear loading, Acta Mater. **138**, 224 (2017).

[66]   X. C. Guo and F. L. Shang, Shear strength and sliding behavior of Ni/Al$_2$O$_3$ interfaces: A first-principle study, J. Mater. Res. **27**, 1237 (2012).

[67]   X. Q. Fu, L. H. Liang, and Y. G. Wei, Atomistic simulation study on the shear behavior of Ag/MgO interface, Comput. Mater. Sci. **155**, 116 (2018).

[68]   X. Y. Guo, Y. Zhang, Y. G. Jung, L. Li, J. Knapp, and J. Zhang, Ideal tensile strength and shear strength of ZrO$_2$(111)/Ni(111) ceramic-metal Interface: A first principle study, Mater. Des. **112**, 254 (2016).

[69]   A. Sazgar, M. R. Movahhedy, M. Mahnama, and S. Sohrabpour, A molecular dynamics study of bond strength and interface conditions in the Al/Al$_2$O$_3$ metal-ceramic composites, Comput. Mater. Sci. **109**, 200 (2015).

[70]   C. R. Dandekar and Y. C. Shin, Molecular dynamics based cohesive zone law for describing Al-SiC interface mechanics, Compos. Part A Appl. Sci. Manuf. **42**, 355 (2011).

[71]   A. Dey, B. A. Baraiya, S. Adhikary, and P. K. Jha, First-Principles Calculations of the Effects of Edge Functionalization and Size on the Band Gap of Be$_3$N$_2$ Nanoribbons: Implications for Nanoelectronic Devices, ACS Appl. Nano Mater. **4**, 493 (2021).

[72]   J. P. Perdew, K. Burke, and M. Ernzerhof, Generalized gradient approximation made simple, Phys. Rev. Lett. **77**, 3865 (1996).

[73]   P. E. Blochl, Projector Augmented-Wave Method, Phys. Rev. B **50**, 17953 (1994).

[74]   M. Suewattana and D. J. Singh, Electronic structure and lattice distortions in PbMg$_{1/3}$Nb$_{2/3}$O$_3$ studied with density functional theory using the linearized augmented plane-wave method, Phys. Rev. B **73** (2006).

[75]   T. Kiguchi, N. Wakiya, K. Shinozaki, and T. J. Konno, Valence-EELS analysis of local electronic and optical properties of PMN-PT epitaxial film, Mater. Sci. Eng. B. **161**, 160 (2009).

[76]   I. I. Oleinik, E. Y. Tsymbal, and D. G. Pettifor, Atomic and electronic structure of Co/SrTiO$_3$/Co magnetic tunnel junctions, Phys. Rev. B **65**, 020401(R) (2002).

[77]   H. J. Monkhorst and J. D. Pack, Special Points for Brillouin-Zone Integrations, Phys. Rev. B **13**, 5188 (1976).

[78]   J. Kim, C. Joh, and Y. Roh, Evaluation of All the Material Constants of PMN-28% PT Piezoelectric Single Crystals for Acoustic Transducers, Sens. Mater. **25**, 539 (2013).

[79]   L. M. Ewart, E. A. Mclaughlin, H. C. Robinson, J. J. Stace, and A. Amin, Mechanical and electromechanical properties of PMNT single crystals for naval sonar transducers, IEEE Trans. Ultrason. Ferroelectr. Freq. Control **54**, 2469 (2007).

[80]   *ABAQUS Version 6.11 Documentation Collection* (Dassault Systèmes Simulia Corp., Providence, RI, USA, 2011).

[81]   L. Y. Jiang, Y. Huang, H. Jiang, G. Ravichandran, H. Gao, K. C. Hwang, and B. Liu, A cohesive law for carbon nanotube/polymer interfaces based on the van der Waals force, J. Mech. Phys. Solids **54**, 2436 (2006).

[82]   G. D. Guo and Y. Zhu, Cohesive-Shear-Lag Modeling of Interfacial Stress Transfer Between a Monolayer Graphene and a Polymer Substrate, J. Appl.Mech. **82**, 031005 (2015).

[83]   M. Safaei, A. Sheidaei, M. Baniassadi, S. Ahzi, M. M. Mashhadi, and F. Pourboghrat, An interfacial debonding-induced damage model for graphite nanoplatelet polymer composites, Comput. Mater. Sci. **96**, 191 (2015).

[84]   S. A. Chowdhury and H. Askari, A unified model for the effective elastic response of inhomogeneities with finite sliding, Int. J. Mech. Sci. **153**, 470 (2019).

[85]   L. L. Shu, X. Y. Wei, T. Pang, X. Yao, and C. L. Wang, Symmetry of flexoelectric coefficients in crystalline medium, J. Appl. Phys. **110**, 104106 (2011).

[86]   J. Narvaez, S. Saremi, J. W. Hong, M. Stengel, and G. Catalan, Large Flexoelectric Anisotropy in Paraelectric Barium Titanate, Phys. Rev. Lett. **115**, 037601 (2015).

[87]   P. Zubko, G. Catalan, A. Buckley, P. R. L. Welche, and J. F. Scott, Strain-gradient-induced polarization in $SrTiO_3$ single crystals, Phys. Rev. Lett. **99**, 167601 (2007).

[88]   W. H. Ma, A study of flexoelectric coupling associated internal electric field and stress in thin film ferroelectrics, Phys. Status Solidi B **245**, 761 (2008).
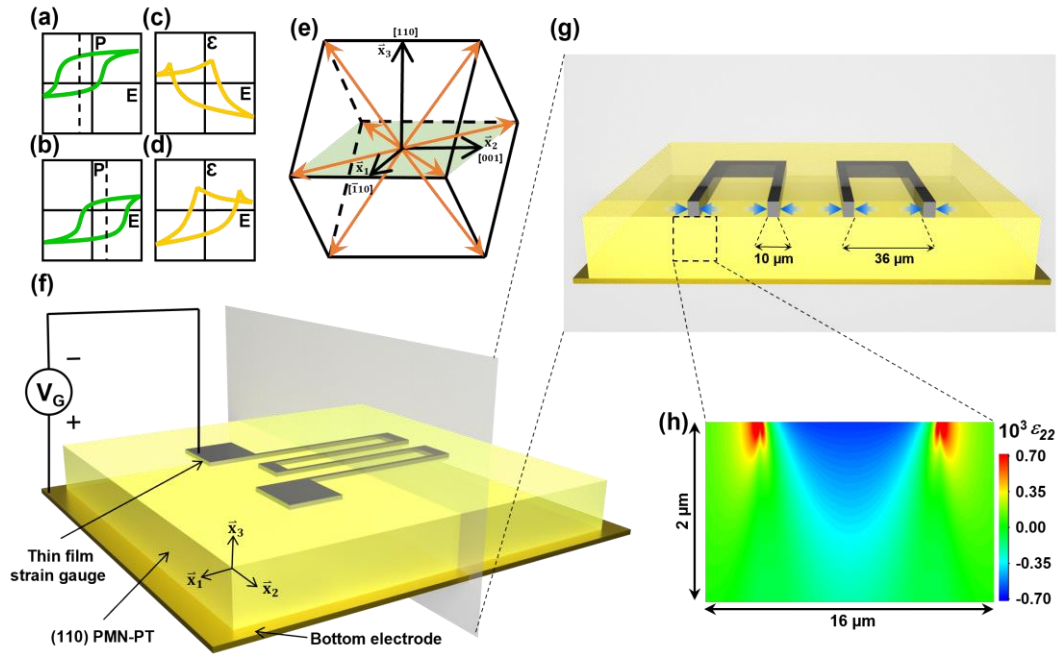
FIG. 1. (a),(b) Ferroelectric polarization hysteresis curves with positive internal bias field and negative internal bias field, respectively. (c),(d) Ferroelastic strain responses correspond to (a) and (b). (e) Rhombohedral unit cell with 8 possible <111> polarization variants of the PMN-PT substrate. (f) Schematic of the device configuration. (g) Schematic of a cross section of the device, where blue arrows represent the film force. (h) A typical strain distribution of the PMN-PT substrate underneath the metal strip.
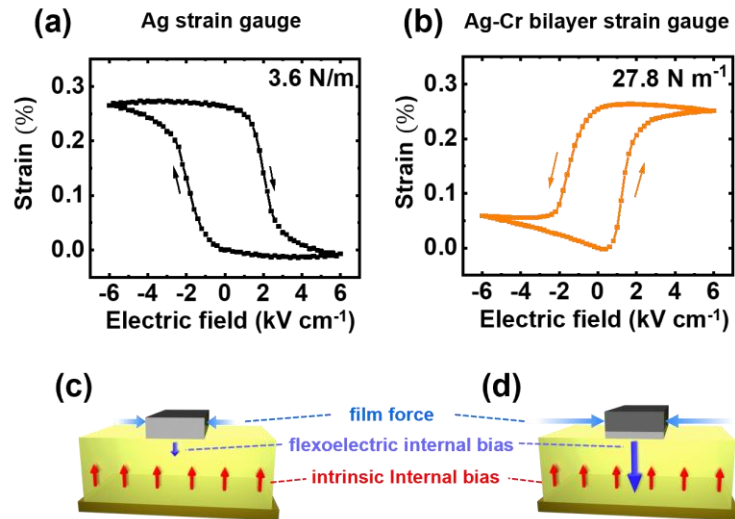
FIG. 2. (a) Strain response of the PMN-PT substrate underneath the Ag alone film with a film force of 3.6 N m^{-1}. (b) Strain response of the PMN-PT substrate underneath the Ag-Cr bilayer film with a film force of 27.8 N m^{-1}. (c),(d) Schematic of the intrinsic internal bias and the flexoelectric effect induced internal bias in the PMN-PT substrate underneath the Ag alone film and the Ag-Cr bilayer film, respectively.
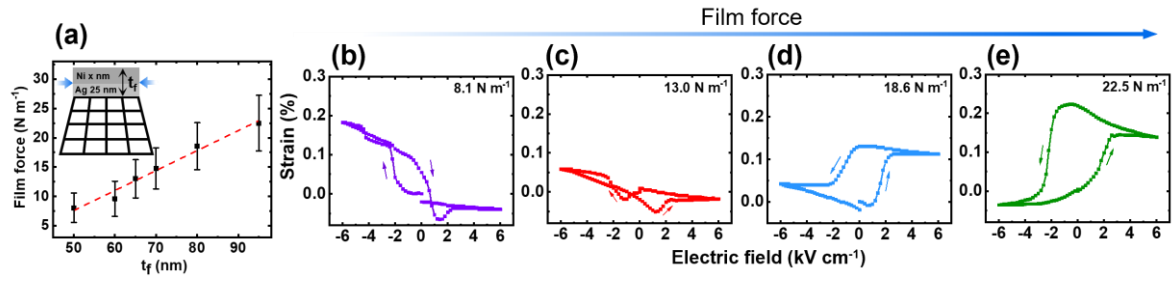
FIG. 3. (a) Film force of the Ag-Ni bilayer film as a function of the film thickness. The Inset shows schematic of the Ag-Ni bilayer film on top of the deformed lattice of the substrate. Blue arrows represent the film force. (b)-(e) Strain response of the PMN-PT substrate underneath the Ag-Ni bilayer film with a film force of 8.1 N m^{-1}, 13.0 N m^{-1}, 18.6 N m^{-1} and 22.5 N m^{-1}, respectively.
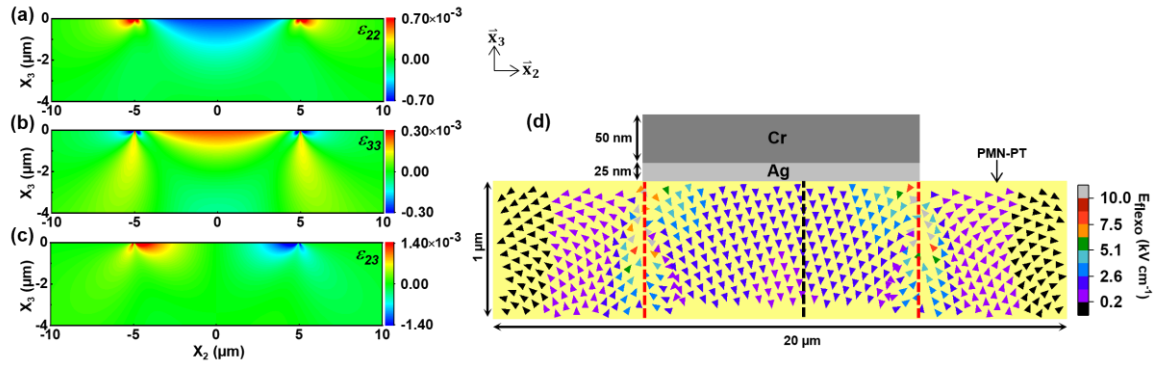
FIG. 4. (a)-(c) FEA simulations of the normal strain ε_{22}, ε_{33} and shear strain ε_{23}, distributions inside the PMN-PT underneath the Ag-Cr bilayer film. (d) Calculated flexoelectric field (E_{flexo}) distribution inside the PMN-PT based on the simulation results of (a), (b) and (c). Here, the direction and the color of each arrow represent the direction and the magnitude of E_{flexo}, respectively. The red dashed lines show where the edges of the Ag-Cr bilayer film locate. The black dashed line shows where the in-plane component of E_{flexo} reverses the direction.
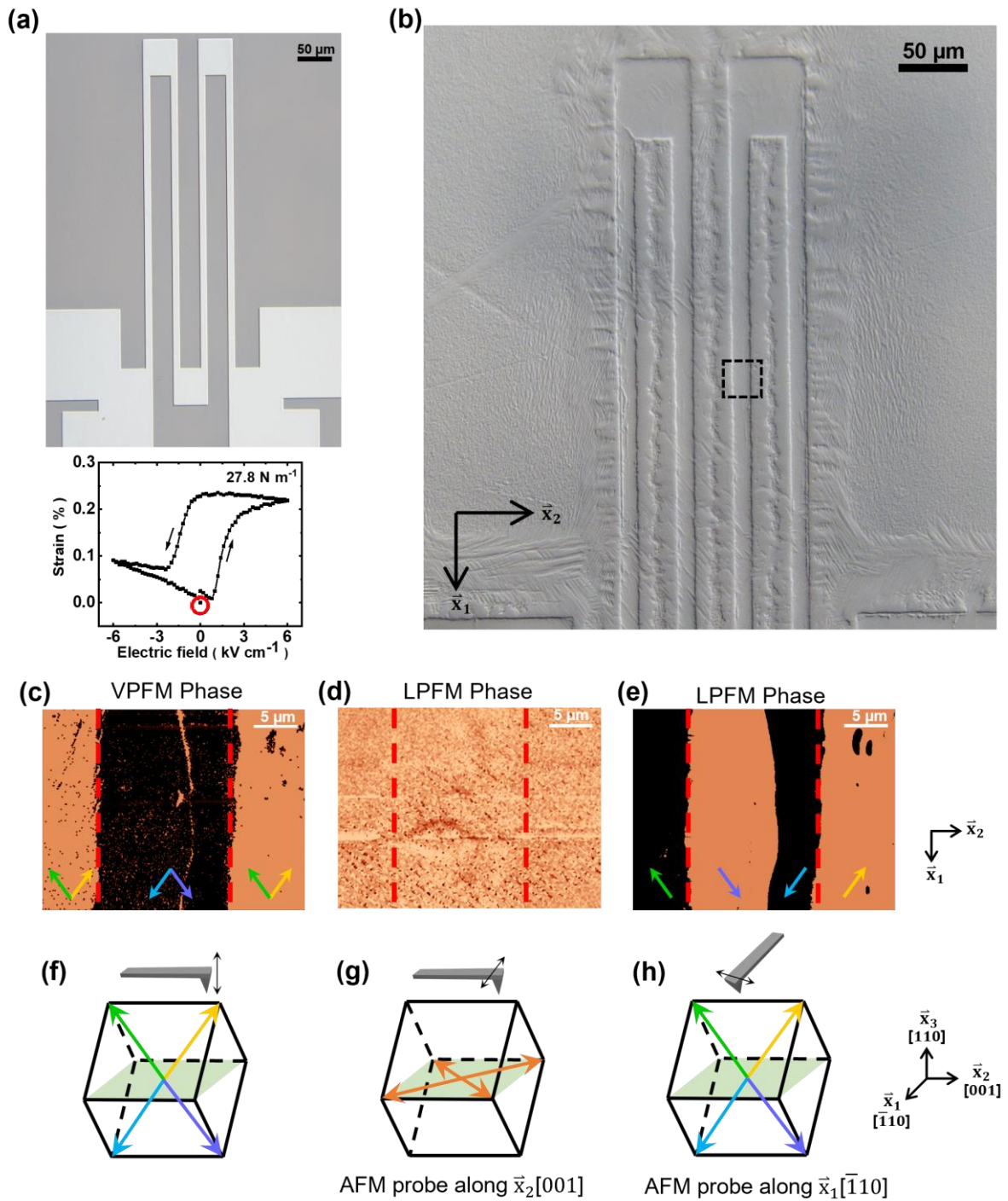
FIG. 5. (a) An optic microscope image of a typical Ag-Cr bilayer film strain gauge and the corresponding strain response. Red circle marked the strain state the device was left after the electric-field cycling. (b) A zoomed-in version of (a) after the relief polishing process under the optic microscope with differential interference contrast (DIC). Dashed square marked the

37

region where the PFM was conducted. (c)-(e) VPFM, LPFM (AFM probe along [001]), and LPFM (AFM probe along [$\bar{1}$10]) phase images. Region between the two red dashed lines is where used to be covered by the metal strip. Colorful arrows at the bottom indicate possible polarization vectors that can result in the corresponding phase result. (f)-(h) Schematics of the polarization vectors that the measurements in (c),(d),(e) are sensitive to with the corresponding probe orientation and vibration mode (marked by the black double-headed arrow) for each PFM measurement, respectively.
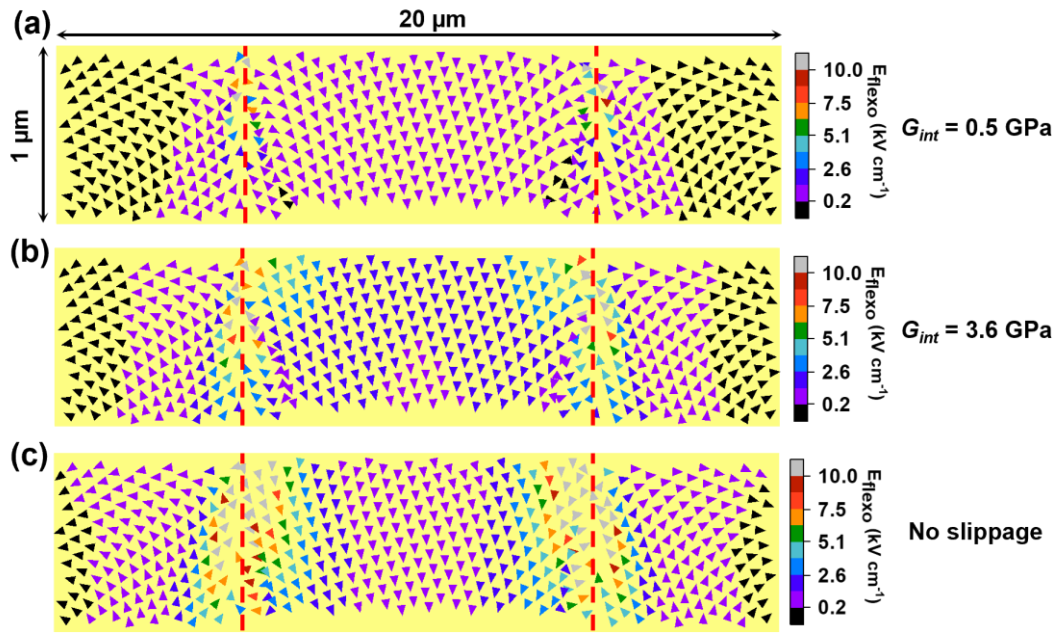
FIG. 6. (a)-(c) Calculated flexoelectric field (E_{flexo}) distribution inside the PMN-PT underneath the Ag-Cr bilayer film based on the assumption of G_{int} = 0.5 GPa, 3.6 GPa, and no slippage, respectively. Here, the direction and the color of each arrow represent the direction and the magnitude of E_{flexo}, respectively. The red dashed lines show where the edges of the Ag-Cr bilayer film are located.